A&A 600, L11 (2017)
DOI: 10.1051/0004-6361/201730736

Astronomy & Astrophysics

Letter to the Editor

The GTC exoplanet transit spectroscopy survey*

VI. Detection of sodium in WASP-52b's cloudy atmosphere

G. Chen[1,2,3], E. Pallé[1,2], L. Nortmann[1,2], F. Murgas[1,2], H. Parviainen[1,2], and G. Nowak[1,2]

[1] Instituto de Astrofísica de Canarias, vía Láctea s/n, 38205 La Laguna, Tenerife, Spain
e-mail: gchen@iac.es
[2] Departamento de Astrofísica, Universidad de La Laguna, Spain
[3] Key Laboratory of Planetary Sciences, Purple Mountain Observatory, Chinese Academy of Sciences, 210008 Nanjing, PR China

Received 6 March 2017 / Accepted 17 March 2017

ABSTRACT

We report the first detection of sodium absorption in the atmosphere of the hot Jupiter WASP-52b. We observed one transit of WASP-52b with the low-resolution Optical System for Imaging and low-Intermediate-Resolution Integrated Spectroscopy (OSIRIS) at the 10.4 m Gran Telescopio Canarias (GTC). The resulting transmission spectrum, covering the wavelength range from 522 nm to 903 nm, is flat and featureless, except for the significant narrow absorption signature at the sodium doublet, which can be explained by an atmosphere in solar composition with clouds at 1 mbar. A cloud-free atmosphere is stringently ruled out. By assessing the absorption depths of sodium in various bin widths, we find that temperature increases towards lower atmospheric pressure levels, with a positive temperature gradient of 0.88 ± 0.65 K km^{-1}, possibly indicative of upper atmospheric heating and a temperature inversion.

Key words. planetary systems – planets and satellites: individual: WASP-52b – planets and satellites: atmospheres – techniques: spectroscopic

1. Introduction

The sodium (Na) and potassium (K) doublets are two of the most important opacity sources for exoplanet atmospheric characterization in the optical wavelengths (Seager & Sasselov 2000), and have been detected in around ten hot giant planets spanning a temperature range of 960−1740 K (e.g., Charbonneau et al. 2002; Redfield et al. 2008; Wood et al. 2011; Sing et al. 2012, 2016; Wyttenbach et al. 2017). Recent ground-based observations have shown the great potential in robust detection and preliminary line-profile diagnosis for Na and K (e.g., Sing et al. 2012; Wyttenbach et al. 2015; Heng et al. 2015; Nikolov et al. 2016).

Here we present WASP-52b as another robust detection to this Na-K sample from our ground-based exoplanet transit spectroscopy survey (e.g., Murgas et al. 2014; Parviainen et al. 2016; Nortmann et al. 2016) with the 10.4 m Gran Telescopio Canarias (GTC). WASP-52b was discovered to transit a K2 dwarf every 1.75 days (Hébrard et al. 2013). This low-density planet (0.43 $M_{\rm Jup}$, 1.25 $R_{\rm Jup}$; Mancini et al. 2017) is highly inflated, and thus well-suited for transmission spectroscopy. The host star is active, and exhibits a rotational modulation of 16.4 ± 0.04 days with an amplitude of 9.6 mmag. Activity signatures such as chromospheric emission in the Ca II H+K lines (Hébrard et al. 2013), occulted star spots (Mancini et al. 2017) and faculae (Kirk et al. 2016) have been identified. Kirk et al. (2016) obtained a broadband transmission spectrum in the u', g' and a 31.2 nm filter centered on Na using the 4.2 m *William Herschel* Telescope, and found an increasing planetary radius towards the red optical.

This paper is organized as follows. In Sect. 2, we summarize the observation and data reduction. In Sect. 3, we present the light-curve analysis and derive the absorption depths at Na and K. In Sect. 4, we discuss the atmospheric properties as indicated by the transmission spectrum and the absorption profile.

2. Observations and data reduction

We observed one transit of the hot Jupiter WASP-52b on the night of August 28, 2015, using the Optical System for Imaging and low-Intermediate-Resolution Integrated Spectroscopy (OSIRIS; Sánchez et al. 2012) mounted at the Nasmyth-B focal station of the GTC.

The observation was carried out in the long-slit mode with the R1000R grism and a 40″-wide slit. The R1000R grism covers a wavelength range of 515−1025 nm with an instrumental dispersion of ~2.6 Å per pixel. The time-series data were collected by two red-optimized 2048 × 4096 Marconi CCDs in the standard 200 kHz and 2 × 2 binning readout mode without windowing, which gives a pixel scale of 0.254″ and an overhead of 23.5 s between two consecutive exposures. A reference star (2MASS 23140726+0839292; r' mag = 11.3) at a separation of 6.5′ was monitored simultaneously with WASP-52 (r' mag = 11.5), and they were placed on different CCD chips.

The transit event was observed from 22:43 UT to 01:25 UT. A total of 308 frames were recorded at an exposure time of 7.5 s. The weather was clear in the first two hours, but became poor after the egress due to cirrus crossing. The moon was 99% illuminated and 30° away. The airmass monotonically decreased from 1.55 to 1.07. The seeing varied between 0.87″ and 1.45″ with a median value of 1.06″, which was measured as the full width at half maximum (FWHM) of the target spatial profile at the central wavelength. This resulted in a seeing limited spectral resolution

* The light curves are only vailable at the CDS via anonymous ftp to cdsarc.u-strasbg.fr (130.79.128.5) or via http://cdsarc.u-strasbg.fr/viz-bin/qcat?J/A+A/600/L11

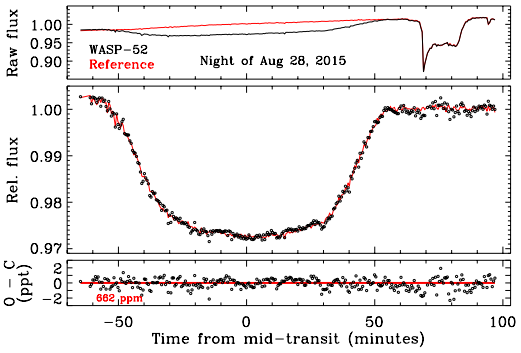

Fig. 1. *Panels from top to bottom*: (1) raw flux of WASP-52 (black line) and the reference star (red line) obtained with GTC/OSIRIS; (2) reference-calibrated light-curve (black circles) and the best-fitting combined model (red line); (3) best-fitting light-curve residuals.

of ∼10 Å. For both spatial and dispersion directions, the positions of spectra remained well within 1 pixel. We did not find any significant rotator-angle-dependent systematics as reported in previous observations (e.g., Nortmann et al. 2016; Chen et al. 2016, 2017), probably because this observation only covered a small range of rotator angles (−229° to −212°).

We reduced the OSIRIS data using the approach outlined in Chen et al. (2016, 2017). The one-dimensional spectra (see Fig. A.1) were extracted using the optimal extraction algorithm (Horne 1986) with an aperture diameter of 24 pixels, which minimized the scatter of the white-color light-curves created from various trial aperture sizes. The time stamp was centered on mid-exposure and converted into the Barycentric dynamical time standard (BJD_{TDB}; Eastman et al. 2010). Any misalignment between the target and reference stars, and any spectral drifts were corrected in the wavelength solutions. Then the requested wavelength range of a given passband was converted to a pixel range, and the flux was summed to generate the time series. The white-color light-curve was integrated from 515 nm to 905 nm, which excluded the range of 755−765 nm to eliminate the noise introduced by the telluric oxygen-A band. Wavelengths redder than 905 nm were not used due to second order contamination and fringing.

3. Analysis

3.1. Light-curve analysis

The light-curve data were fit by a model that combines both transit (Mandel & Agol 2002) and systematics in a multiplicative form, as detailed in Chen et al. (2016, 2017). The combined model was parameterized as mid-transit time (T_{mid}), orbital inclination (i), scaled semi-major axis ($a/R_\star$), planet-to-star radius ratio ($R_p/R_\star$), quadratic limb-darkening coefficients (u_1, u_2), and coefficients of systematics models (c_j). A circular orbit was assumed and the orbital period was fixed. The limb-darkening coefficients were always imposed with Gaussian priors ($u_i \pm 0.1$), whose values were calculated using the Python package written by Espinoza & Jordán (2015) with the stellar parameters (T_{eff}, $\log g$, [Fe/H]) from Hébrard et al. (2013). A customized version of the Transit Analysis Package (TAP; Gazak et al. 2012) was employed to perform the Markov chain Monte Carlo analysis to find the best-fitting parameters and associated uncertainties, which accounted for the correlated noise using a wavelet-based likelihood function (Carter & Winn 2009).

Table 1. System parameters.

Parameter	Value
P [days]	1.7497798 (fixed)
e	0 (fixed)
T_{mid} [BJD_{TDB}]	2 457 263.49829 ± 0.00016
i [°]	85.06 ± 0.27
$a/R_\star$	7.14 ± 0.12
$R_p/R_\star$	0.1608 ± 0.0018
u_1	0.443 ± 0.069
u_2	0.147 ± 0.091

We first fit the white-color light-curve to derive the overall transit parameters (see Table 1 and Fig. 1). The systematics model was a linear combination of spatial FWHM and airmass, which was chosen by the Bayesian information criterion (BIC; Schwarz 1978). The resulting transit parameters agree well with previous studies (Hébrard et al. 2013; Kirk et al. 2016; Mancini et al. 2017), except for $R_p/R_\star$, which appears shallower than previously reported. This deviation is probably caused by stellar activity, given that occulted star spots (Mancini et al. 2017) and faculae (Kirk et al. 2016) have been identified several times.

We then fit the spectroscopic light-curves to derive the transmission spectrum. A common-mode trend was removed from all the spectroscopic light-curves, which was derived after dividing the white-color light-curve by the best-fitting transit model. The remaining wavelength-dependent effects were characterized by a linear trend of time. The values of (i, $a/R_\star$, T_{mid}) were fixed to the ones listed in Table 1. Two sets of transmission spectra were derived: (1) 22 bins of width 16.5 nm outside of Na and K, 3 bins of 16 Å centered on Na and K, and 1 bin of 18 Å in-between the K doublet; (2) regions outside of Na and K also divided into bins of width 16 Å. Set 2 provides uniform narrow bins as a double check for Set 1. We present Set 1 spectroscopic light-curves in Fig. A.2 and their transit depths in Table A.1 in the appendix. The standard deviation of white and spectroscopic light-curve residuals were typically 3.3× and 1.00−1.33× photon noise, respectively.

The transit depth at the Na line ($R_p/R_\star = 0.1717 \pm 0.0030$) is significantly larger than the rest of the 16 + 18 Å transit depths, which have an almost Gaussian distribution around $R_p/R_\star = 0.1608$. We show the Hα line as a control example in Fig. 2. Excluding the transit depths of Na and K, we fit a horizontal line to the continuum to estimate the significance of deviation, and found 3.6σ for Na, 2.2σ for K D_2, 0.9σ for K D_1, and 2.2σ for K D_2+D_1 combined.

3.2. Integrated absorption depth

Following the approach of Charbonneau et al. (2002), we derived the integrated absorption depth (AD) for the Na line, similar to the methodology in Sing et al. (2008), Vidal-Madjar et al. (2011b), Huitson et al. (2012), for example. We created reference-calibrated light-curves for one band centered on Na (5893 Å) and two bands bracketing this central band (5818−5843 Å and 5943−5968 Å). Each spectroscopic light-curve was modeled in the same way as outlined in Sect. 3.1. After removing the systematics trends and limb-darkening effects, we divided the corrected central-band light-curve by the mean

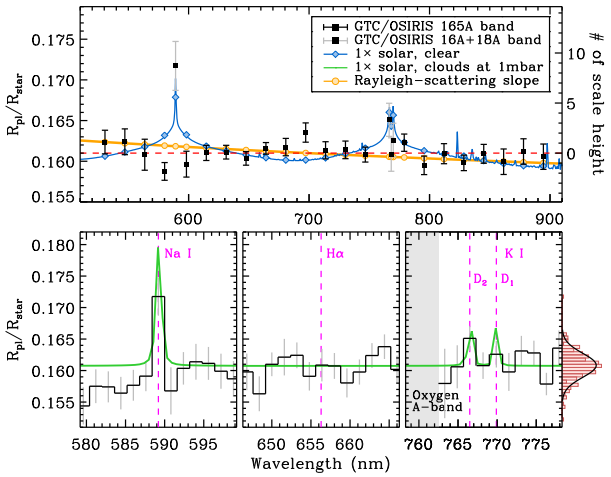

Fig. 2. GTC/OSIRIS transmission spectrum of WASP-52b. *Top panel*: the transmission spectrum composed of 22 bins of 16.5 nm (black squares with black error bars), 3 bins of 16 Å centered on Na and K, and 1 bin of 18 Å in-between the K doublet (black squares with gray error bars). The blue line shows a 1300 K 1× solar cloud-free model (Kempton et al. 2017). The orange line shows a Rayleigh-scattering model ($\alpha = -4$). The red dashed line shows a flat line at $R_p/R_\star = 0.1608$. *Bottom panels*: the close-up of Na, Hα, and K lines (black histogram with gray error bars) in bins of 16 Å (or 18 Å). The green line shows a 2700 K 1× solar atmosphere with the clouds at 1 mbar. The red histogram on the right shows the distribution of all the 16 + 18 Å transit depths.

of the corrected bracketing-band light-curves, and derived the AD in the same way as Charbonneau et al. (2002). The central band has bin widths varying from 16 Å to 88 Å in increasements of 4 Å. We did not use bin widths narrower than 16 Å, which would be below the seeing-limited spectral resolution. As shown in Fig. 3, the integrated Na AD drops quickly with increasing bin widths until ~36 Å, and then slowly approaches a flat continuum, where the largest AD is in the 16 Å bin ($\Delta F/F = 0.00378 \pm 0.00068$). This indicates that the core of the Na line is very narrow.

We also derived the AD for the K doublet (D_2: 7665 Å; D_1: 7699 Å) individually. Due to the sharp and strong oxygen-A band, we were not able to construct the bracketing bands directly neighboring the central band, which were instead set as 7462−7512 Å and 7852−7902 Å. Since the K D_1 line is almost indistinguishable from the neighboring wavelengths (see Fig. 2), its AD is heavily contaminated by the neighbors at larger bin widths. On the other hand, the K D_2 line, which was 2.2σ higher than the continuum, shows a similar AD profile to the Na line (see Fig. 3), where the largest AD is also in the 16 Å bin ($\Delta F/F = 0.00149 \pm 0.00049$).

4. Discussion

4.1. Transmission spectrum

As shown in Fig. 2, the derived GTC/OSIRIS transmission spectrum for WASP-52b does not exhibit any broad spectral signatures, except for the narrow excess absorption at the Na line. The standard deviation of the 16.5 nm transit depths $\sigma(R_p/R_\star) = 0.00110$ is smaller than one atmospheric scale height $H/R_\star = kT/(\mu g R_\star) = 0.00126$, where the stellar radius $R_\star = 0.786\ R_\odot$, the planetary surface gravity $g = 6.85$ m s^{-2} and the planetary equilibrium temperature $T_{eq} = 1315$ K were taken from Mancini et al. (2017); k is the Boltzmann constant; μ is the mean molecular weight (MMW) and assumed as 2.3× proton mass.

We fit a horizontal line with a constant value and a line with a slope in the ($\ln\lambda$, $R_p/R_\star$) space to the 16.5 nm transit depths, corresponding to (i) clouds with particles comparable to or larger than the probed wavelengths and (ii) clouds with small particles, respectively. The horizontal fit resulted in a slightly larger χ^2 value, but it had a ΔBIC = 2.9 lower than the slope fit. For the slope fit, we obtained

$$\alpha T = \frac{\mu g}{k}\frac{dR_p}{d\ln\lambda} = -873 \pm 1824\ \mathrm{K}, \quad (1)$$

where α is the index of the power law cross-section $\sigma = \sigma_0(\lambda/\lambda_0)^\alpha$ for the atmospheric opacity sources (Lecavelier Des Etangs et al. 2008) and $\alpha = -4$ corresponds to Rayleigh scattering. With $T = T_{eq}$ and $\mu = 2.3 m_H$, we calculated $\alpha = -0.7 \pm 1.4$, which deviates from −4 at 2.4σ and indicates that the cloud particles are not likely small.

To distinguish between clear and cloudy scenarios, we also computed isothermal atmospheric models of different temperatures and metallicities with clouds at different pressure levels using the `Exo-Transmit` code (Kempton et al. 2017), which were compared to our transmission spectrum (22 bins of 16.5 nm and 4 bins of 16 + 18 Å). Atmospheric models with clouds at the pressure of 1 mbar ranked higher in the χ^2 statistics. In Fig. 2, we show the 1× solar cloud-free model in the top panel, and show one of the best atmospheric models (2700 K, 1× solar, clouds at 1 mbar) in the bottom panels. These two models have a reduced chi-square of $\chi^2_r = 2.09$ and 0.79 (d.o.f. = 25), respectively. For comparison, the fit of a horizontal line results in $\chi^2_r = 1.42$.

We calculated the cloudiness index C following the approach of Heng (2016), which was based on measuring the transit radii at the line center and wing of the Na/K lines, with the cloud-free atmosphere being at $C = 1$. For WASP-52b, the cloudiness index is $C_{Na} = 5.3 \pm 3.0$ based on the Na line, and $C_K = 6.9 \pm 3.8$ based on the K D_2 line. We used the 28 and 16 Å bins for Na and K, respectively, which enables us to compare our results with HAT-P-1b ($C_{Na} = 5.5 \pm 2.7$, $C_K = 8.5 \pm 7.9$; Heng 2016). These two planets have almost the same equilibrium temperature, mass, radius, surface gravity, and happen to have the same cloudiness index, but the host star WASP-52 (K2V) is far more active than HAT-P-1 (G0V), making them good comparative targets for the origin of clouds.

We note that, in principle, the best-fitting slope in the transmission spectrum can be introduced by unocculted star spots or occulted faculae, which would indicate shallower true transit depths than currently measured. However, the correlated noise in our white-color light-curve, which might arise from occulted star spots or occulted faculae, does not show any dependency of wavelength (see Fig. A.2). Furthermore, we do not observe any excess or deficient absorption in other stellar lines (e.g., Hα, Ca II IRT). Therefore, we argue that the excess Na absorption is not likely a contamination of stellar activity.

4.2. Thermal structure for the upper atmosphere

Vidal-Madjar et al. (2011b,a) and Huitson et al. (2012) have derived the temperature structures for the upper atmospheres of HD 209458b and HD 189733b by investigating the Na AD profile. We followed the approach outlined in Huitson et al. (2012) to generate isothermal models for the Na and K lines. The model was binned in the same way in which we created the AD profile.

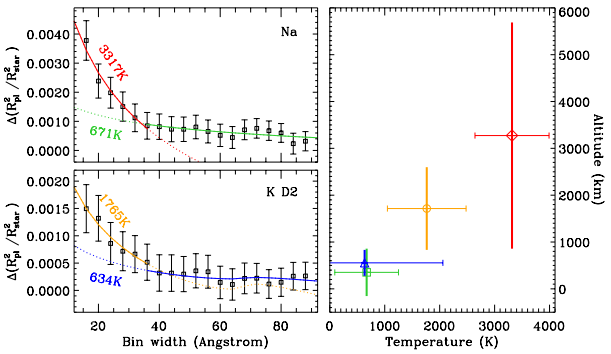

Fig. 3. *Left panels*: absorption depths integrated in different bin widths for Na (*top*) and K D_2 (*bottom*). The red/orange (green/blue) curves present the best-fitting isothermal models for the core (wing) region. *Right panel*: temperatures of these isothermal models at corresponding altitude ranges.

Given the discussion in Sect. 4.1, we assumed the pressure at the reference level to be 1 mbar, the Na and K abundances to be 1× solar, and the planet radius to be $R_p/R_\star = 0.1608$ (i.e., the continuum altitude). Assuming that the probed altitude range is isothermal, the slope of the AD profile is a function of temperature, similar to the case of Rayleigh scattering.

We fit the model to the bin width ranges of 16−36 Å and 40−88 Å, corresponding to the line core and wings, respectively. The results are shown in Fig. 3. The temperatures inferred from the line wings of Na and K are almost the same ($T \approx 665$ K), while the Na line core has a much higher temperature ($T = 3320 \pm 670$ K) than the K D_2 core ($T = 1765 \pm 715$ K) as a result of a wider and higher probed altitude range. However, it is possible that the Na core temperature is overestimated due to decreasing MMW at higher altitude (e.g., Yelle 2004; García Muñoz 2007). Assuming a constant $\mu = 2.3\ m_H$ over all altitudes, we estimated that the Na line probed a pressure range of 1500−87 μbar at the wing and 87–5 μbar at the core, and the K D_2 line probed 430−82 mbar at the wing and 82−12 μbar at the core, individually. Therefore, the inferred average temperature-pressure profile of WASP-52b shows an increasing trend towards higher upper atmosphere, with a positive temperature gradient of 0.88 ± 0.65 K km^{-1}, which is similar to HD 209458b (Vidal-Madjar et al. 2011b,a), HD 189733b (Huitson et al. 2012; Heng et al. 2015), and WASP-49b (Wyttenbach et al. 2017), and might be indicative of upper atmospheric heating and escaping processes (e.g., Lammer et al. 2003; Lecavelier des Etangs et al. 2004; Koskinen et al. 2013a,b). This also suggests WASP-52b as a potential candidate of evaporating planets (e.g., Vidal-Madjar et al. 2003; Lecavelier Des Etangs et al. 2010; Ehrenreich et al. 2015).

On the other hand, as pointed out by Huitson et al. (2012), the integrated AD profile could be compromised by the dilution effects of increasing bandwidth around an unresolved line. Therefore, future observations of high-resolution spectroscopy are required to confirm this line-profile diagnosis, which could also provide useful information on the impact of stellar activity.

5. Conclusions

We have observed one transit of WASP-52b with GTC/OSIRIS. The resulting transmission spectrum does not show any broad spectral signature except for a prominent and narrow excess absorption at the Na line, indicative of a cloudy atmosphere. The integrated absorption depth profile of Na and K might suggest an inverted temperature structure for the upper atmosphere. Future ground-based high-resolution spectroscopy is required to put further constraints on line-profile diagnosis and stellar activity.

Acknowledgements. The authors thank the referee K. Heng for useful and constructive comments. This research is based on observations made with the Gran Telescopio Canarias (GTC), installed in the Spanish Observatorio del Roque de los Muchachos, operated on the island of La Palma by the Instituto de Astrofísica de Canarias. This work is partly financed by the Spanish Ministry of Economics and Competitiveness through projects ESP2013-48391-C4-2-R, ESP2014-57495-C2-1-R, and AYA2012-39346-C02-02. G.C. also acknowledges the support by the National Natural Science Foundation of China (Grant No. 11503088) and the Natural Science Foundation of Jiangsu Province (Grant No. BK20151051). This research has made use of the VizieR catalogue access tool, CDS, Strasbourg, France (Wenger et al. 2000).

References

Carter, J. A., & Winn, J. N. 2009, ApJ, 704, 51
Charbonneau, D., Brown, T. M., Noyes, R. W., & Gilliland, R. L. 2002, ApJ, 568, 377
Chen, G., Palle, E., Murgas, F., et al. 2016, A&A, submitted
Chen, G., Guenther, E. W., Palle, E., et al. 2017, A&A, 600, A138
Eastman, J., Siverd, R., & Gaudi, B. S. 2010, PASP, 122, 935
Ehrenreich, D., Bourrier, V., Wheatley, P. J., et al. 2015, Nature, 522, 459
Espinoza, N., & Jordán, A. 2015, MNRAS, 450, 1879
García Muñoz, A. 2007, Planet. Space Sci., 55, 1426
Gazak, J. Z., Johnson, J. A., Tonry, J., et al. 2012, Adv. Astron., 2012, 30
Hébrard, G., Collier Cameron, A., Brown, D. J. A., et al. 2013, A&A, 549, A134
Heng, K. 2016, ApJ, 826, L16
Heng, K., Wyttenbach, A., Lavie, B., et al. 2015, ApJ, 803, L9
Horne, K. 1986, PASP, 98, 609
Huitson, C. M., Sing, D. K., Vidal-Madjar, A., et al. 2012, MNRAS, 422, 2477
Kempton, E. M.-R., Lupu, R. E., Owusu-Asare, A., Slough, P., & Cale, B. 2017, PASP, 129, 044402
Kirk, J., Wheatley, P. J., Louden, T., et al. 2016, MNRAS, 463, 2922
Koskinen, T. T., Harris, M. J., Yelle, R. V., & Lavvas, P. 2013a, Icarus, 226, 1678
Koskinen, T. T., Yelle, R. V., Harris, M. J., & Lavvas, P. 2013b, Icarus, 226, 1695
Lammer, H., Selsis, F., Ribas, I., et al. 2003, ApJ, 598, L121
Lecavelier des Etangs, A., Vidal-Madjar, A., McConnell, J. C., & Hébrard, G. 2004, A&A, 418, L1
Lecavelier Des Etangs, A., Pont, F., Vidal-Madjar, A., & Sing, D. 2008, A&A, 481, L83
Lecavelier Des Etangs, A., Ehrenreich, D., Vidal-Madjar, A., et al. 2010, A&A, 514, A72
Mancini, L., Southworth, J., Raia, G., et al. 2017, MNRAS, 465, 843
Mandel, K., & Agol, E. 2002, ApJ, 580, L171
Murgas, F., Pallé, E., Zapatero Osorio, M. R., et al. 2014, A&A, 563, A41
Nikolov, N., Sing, D. K., Gibson, N. P., et al. 2016, ApJ, 832, 191
Nortmann, L., Pallé, E., Murgas, F., et al. 2016, A&A, 594, A65
Parviainen, H., Pallé, E., Nortmann, L., et al. 2016, A&A, 585, A114
Redfield, S., Endl, M., Cochran, W. D., & Koesterke, L. 2008, ApJ, 673, L87
Sánchez, B., Aguiar-González, M., Barreto, R., et al. 2012, in SPIE Confe. Ser., 8446, 4
Schwarz, G. 1978, Ann. Stat., 6, 461
Seager, S., & Sasselov, D. D. 2000, ApJ, 537, 916
Sing, D. K., Vidal-Madjar, A., Désert, J.-M., Lecavelier des Etangs, A., & Ballester, G. 2008, ApJ, 686, 658
Sing, D. K., Huitson, C. M., Lopez-Morales, M., et al. 2012, MNRAS, 426, 1663
Sing, D. K., Fortney, J. J., Nikolov, N., et al. 2016, Nature, 529, 59
Vidal-Madjar, A., Lecavelier des Etangs, A., Désert, J.-M., et al. 2003, Nature, 422, 143
Vidal-Madjar, A., Huitson, C. M., Lecavelier Des Etangs, A., et al. 2011a, A&A, 533, C4
Vidal-Madjar, A., Sing, D. K., Lecavelier Des Etangs, A., et al. 2011b, A&A, 527, A110
Wenger, M., Ochsenbein, F., Egret, D., et al. 2000, A&AS, 143, 9
Wood, P. L., Maxted, P. F. L., Smalley, B., & Iro, N. 2011, MNRAS, 412, 2376
Wyttenbach, A., Ehrenreich, D., Lovis, C., Udry, S., & Pepe, F. 2015, A&A, 577, A62
Wyttenbach, A., Lovis, C., Ehrenreich, D., et al. 2017, A&A, in press, DOI: 10.1051/0004-6361/201630063
Yelle, R. V. 2004, Icarus, 170, 167

Appendix A: Additional figures and table

In this appendix, we show the example stellar spectra in Fig. A.1, the spectroscopic light-curves in Fig. A.2, and the derived wavelength-dependent transit depths in Table A.1.

Table A.1. Transmission spectrum obtained with GTC/OSIRIS.

#	Wavelength (Å)		$R_p/R_\star$
	Center	Width	
1	5306	165	0.1624 ± 0.0015
2	5471	165	0.1624 ± 0.0016
3	5636	165	0.1608 ± 0.0019
4	5800	165	0.1588 ± 0.0011
5	5891	16	0.1717 ± 0.0030
6	5981	165	0.1596 ± 0.0016
7	6147	165	0.1610 ± 0.0009
8	6312	165	0.1611 ± 0.0008
9	6477	165	0.1604 ± 0.0008
10	6642	165	0.1616 ± 0.0007
11	6807	165	0.1617 ± 0.0011
12	6972	165	0.1635 ± 0.0012
13	7137	165	0.1613 ± 0.0011
14	7302	165	0.1614 ± 0.0011
15	7467	165	0.1608 ± 0.0009
16	7665	16	0.1651 ± 0.0020
17	7682	18	0.1608 ± 0.0021
18	7699	16	0.1626 ± 0.0021
19	7790	165	0.1623 ± 0.0011
20	7955	165	0.1595 ± 0.0011
21	8120	165	0.1609 ± 0.0012
22	8285	165	0.1598 ± 0.0010
23	8450	165	0.1609 ± 0.0012
24	8615	165	0.1599 ± 0.0016
25	8780	165	0.1612 ± 0.0016
26	8945	165	0.1606 ± 0.0016

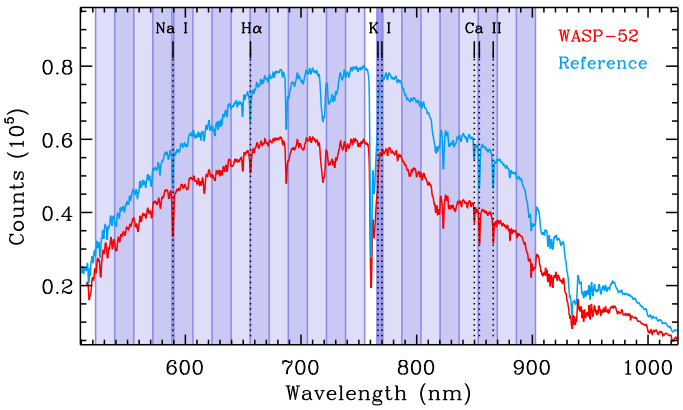

Fig. A.1. Example stellar spectra of WASP-52 (red) and the reference star (blue) obtained with the R1000R grism of GTC/OSIRIS on the night of August 28, 2015. The color-shaded areas indicate the divided passbands that are used to create the spectroscopic light-curves.

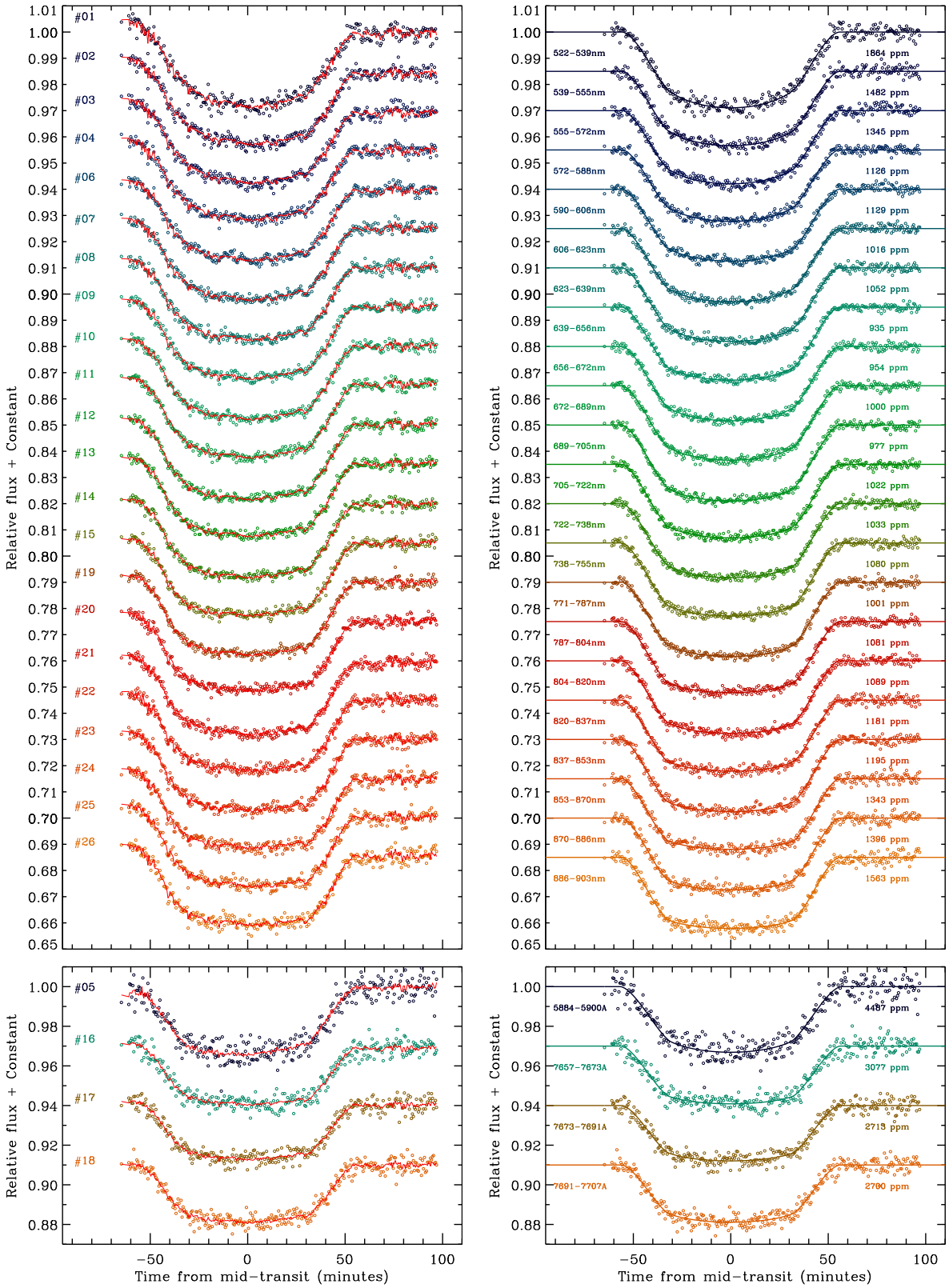

Fig. A.2. Raw (*left panel*) and detrended (*right panel*) spectroscopic light-curves of WASP-52b obtained with the R1000R grism of GTC/OSIRIS, including 22 channels of 16.5 nm, 3 channels of 16 Å, and 1 channel of 18 Å, as indicated in Fig. A.1. For clarity, the four narrow-band light-curves are shown separately in the *bottom panels*.